COMMUNICATION

Complex Oxide–Noble Metal Conjugated Nanoparticles

Jun-Ling Guo, Yao-De Chiou, Wen-I Liang, Heng-Jui Liu, Ying-Jiun Chen, Wei-Cheng Kuo, Chih-Ya Tsai, Kai-An Tsai, Ho-Hung Kuo, Wen-Feng Hsieh, Jenh-Yih Juang, Yung-Jung Hsu, Hong-Ji Lin, Chien-Te Chen, Xue-Pin Liao, Bi Shi, and Ying-Hao Chu*

The past decade has witnessed tremendous progress in the synthesis of nanoparticles (NPs) with controllable size, shape, and composition.[1,2] However, these NPs would unlikely meet the rising demand for the advanced breeds of building blocks for functional materials and devices.[3] Hybrid NPs composed of multiple components usually exhibit multiple functionalities. These NPs attract tremendous research interest because of their unique properties and applications that, however, are difficult (or even impossible) to be achieved by single-component NPs.[4–6] To date, significant progress has been achieved in the synthesis of noble metal NPs with epitaxial unitary, binary domain hybrid NPs (eg., Au@Ni, Au–Fe$_3$O$_4$, Au–TiO$_2$, and Au–CdSe) by using various synthetic methods including surface selective modification,[5] template-assisted self-assembly,[6] phase separation,[7] and surface-controlled nucleation and growth.[8] However, almost all of these methods involve the use of environmentally harmful chemicals (precursor, surfactant, and solvent) and complicated synthetic procedures, which inevitably hinders the applicability of these products. Complex oxides cover a broad spectrum of intriguing functionalities due to the interplay among the lattice, charge, orbit, and spin degrees of freedom. Heterostructures containing complex oxides provide a powerful route to manipulate these degrees of freedom and offer tremendous opportunities for next-generation electronic devices.[9–12] However, using conventional methods to synthesize complex oxides with small size and high crystallinity is very difficult (due to the extremely

strict requirements of well matching reaction rates of multiple precursors), and combining them with noble metals in hybrid NP structures even presents a greater challenge. Among various complex oxides, complex oxide NPs with a spinel structure (e.g., CoFe$_2$O$_4$, MnFe$_2$O$_4$, NiFe$_2$O$_4$) show remarkable optical, electronic, mechanical, thermal, and magnetic properties.[13,14] These properties are exploited in technological applications like ferrofluids,[15] biomedicine,[16] and recording media.[17] On the other hand, as a large family of complex oxides, perovskites (e.g., SrTiO$_3$, BiFeO$_3$, LaMnO$_3$) also draw wide-spread attention due to their catalytic,[18] ferroelectric,[19] and ferromagnetic properties,[20] as well as their application in superconductors,[21] thermoelectrics,[22] and fuel cells.[23] Nanometer-scaled perovskites even exhibit distinct properties over bulk materials, such as quantum paraelectrics[24] and photoluminescence.[25] In this study, a simple yet versatile strategy to synthesize complex oxide–noble metal hybrid NPs is demonstrated. As model hybrid NPs, gold–spinel heterodimer (Au-CoFe$_2$O$_4$) and gold–pervoskite heterodimer (Au-SrTiO$_3$) NPs were fabricated. We examined these NPs structurally and chemically by a combination of X-ray diffraction, Raman spectroscopy, synchrotron radiation X-ray absorption, and X-ray photoelectron spectroscopy. The interplay between complex oxides and noble metals is explored based on the magnetic, plasmonic, and photocatalyic behaviors of these NPs. Our study paves the way to the intriguing functionalities of complex oxide conjugation.

The synthesis of hybrid NPs is shown in **Figure 1**. This approach allows ready control of the domain size of the Au NPs (Figure 1a) and their in situ conjugation with complex oxide NPs generated by a pulsed laser ablation in liquid (PLAL) process. Firstly, we synthesized Au NPs with various size (3–15 nm) based on a solution method, the details can be found in the experimental section.[26] The solution with gold NPs was then used in a PLAL process. The PLAL growth process is depicted schematically in Figure 1b. When the laser irradiates the target in a liquid, the local area around the laser spot can be ablated, followed by the formation of a primary metal-droplet region.[27] The species are highly confined by the surrounding liquid, leading to the formation of a plasma region.[28] Simultaneously, the surrounding Au NPs serve as heterogeneous nucleation sites of complex oxides to form the heterodimer hybrids with well-defined structure and composition. On the basis of the above interfacial interaction, such a pulsed laser-assisted nanoparticle-conjunction process can be extended to other noble metal/complex oxide systems, due to the tremendous versatility of the PLAL process.

In order to show the versatility of the PLAL process, SrTiO$_3$ perovskite and CoFe$_2$O$_4$ spinel were selected in this study.

J.-L. Guo, Y.-D. Chiou, W.-I. Liang, H.-J. Liu, K.-A. Tsai, Dr. H.-H. Kuo, Prof. Y.-J. Hsu, Prof. Y.-H. Chu
Department of Materials Science and Engineering
National Chiao Tung University
HsinChu, 30010, Taiwan, ROC
E-mail: yhc@nctu.edu.tw

J.-L. Guo, Prof. X.-P. Liao, Prof. B. Shi
Department of Biomass Chemistry and Engineering
Sichuan University
Chengdu, 610000, P. R. China

Y.-J. Chen, Dr. H.-J. Lin, Dr. C.-T. Chen
National Synchrotron Radiation Research Center
HsinChu, 30010, Taiwan, ROC

W.-C. Kuo, Prof. J.-Y. Juang
Department of Electrophysics
National Chiao Tung University
HsinChu, 30010, Taiwan, ROC

C.-Y. Tsai, Prof. W.-F. Hsieh
Department of Photonics and Institute of
Electro-Optical Engineering
National Chiao Tung University
HsinChu, 30010, Taiwan, ROC

Materials
Views
www.MaterialsViews.com

ADVANCED
MATERIALS
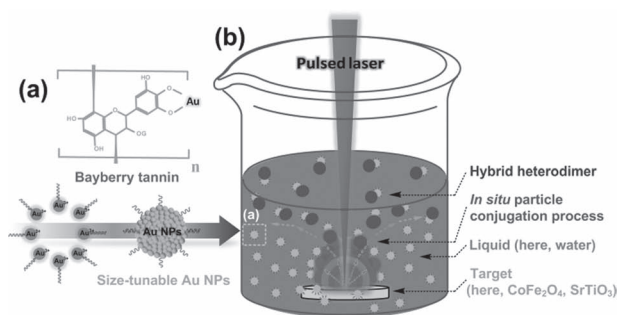www.advmat.de

COMMUNICATION

Figure 1. Schematic diagram shows the one-step in situ particle-conjugation process.

The morphology, particle size, and chemical information of the as-prepared Au–CoFe$_2$O$_4$ and Au–SrTiO$_3$ hybrid NPs were analyzed by energy dispersive X-ray spectroscopy (EDX)-assisted transmission electron microscopy (TEM), as shown in **Figure 2**. It is clear that both of these hybrids are characteristic of a heterodimer structure as evidenced by EDX analysis. The Au domains appear deeper in contrast than CoFe$_2$O$_4$ (Figure 2a) or SrTiO$_3$ (Figure 2e). As shown in the inset line profiles of Figure 2a and 2e, the EDX line-scan analysis clearly shows strong Au element signals in the dark region, while strong Fe or Ti element signals appear in the light colored region in CoFe$_2$O$_4$ and SrTiO$_3$ domains. The EDX elemental mapping of Au and Fe (as shown in Figure 2b) further confirms the heterodimer structure of Au–CoFe$_2$O$_4$ NPs. High resolution TEM (HRTEM) images are also used to investigate the crystallinity of these as-prepared hybrids. Figure 2c and 2f show the HRTEM images and Figure 2d and 2g are the corresponding fast Fourier transform

(FFT), respectively. In the case of Au–CoFe$_2$O$_4$, it is noticed that some clear lattice fringes with a spacing of 2.3 Å can be observed in the dark region, which corresponds to the {111} planes of face-centered cubic (fcc) structured Au. Meanwhile, the lattice fringes with a spacing of 4.8 Å can be observed in the light colored region, which could be indexed to the {111} planes of spinel structured CoFe$_2$O$_4$.[29] In the case of Au–SrTiO$_3$ (Figure 2e and 2f), the lattice was measured to be 2.3 Å for the noble metal particles, indicating the {111} planes of the fcc structured Au; while the lattice fringes with a spacing of 2.8 Å can be found in the light color region, which could be assigned to the {110} planes of the perovskite structured SrTiO$_3$.[30] The structure was also investigated macroscopically by X-ray diffraction (XRD) (Figure S1, Supporting Information) and Raman spectroscopy (Figure S2, Supporting Information), which, again, confirm the structural symmetry of the as-prepared hybrids. The details of the structural identification can be found in the Supporting Information. After confirmation of the microstructure, the portion variation of hybrid NPs is also demonstrated in Figure 2h (with a Au diameter around 3 nm) and 2i (with a Au diameter around 15 nm), leading to the morphology change of the hybrid NPs. Notably, it has been pointed out that the morphology variation of the hybrid might alter its electronic properties, which may lead to controllable and new properties.[31] However, it is also important to point out that the PLAL method has a shortage regarding the size distribution of synthesized nanostructures. In addition, it is also shown that the PLAL-based conjunction process in the present study leads to a lack of uniformity in the achieved products due to the observation that some of the Au seeds and PLAL-generated oxide NPs show a single domain without epitaxial structure. Therefore, further attempts are certainly needed to overcome these problems.
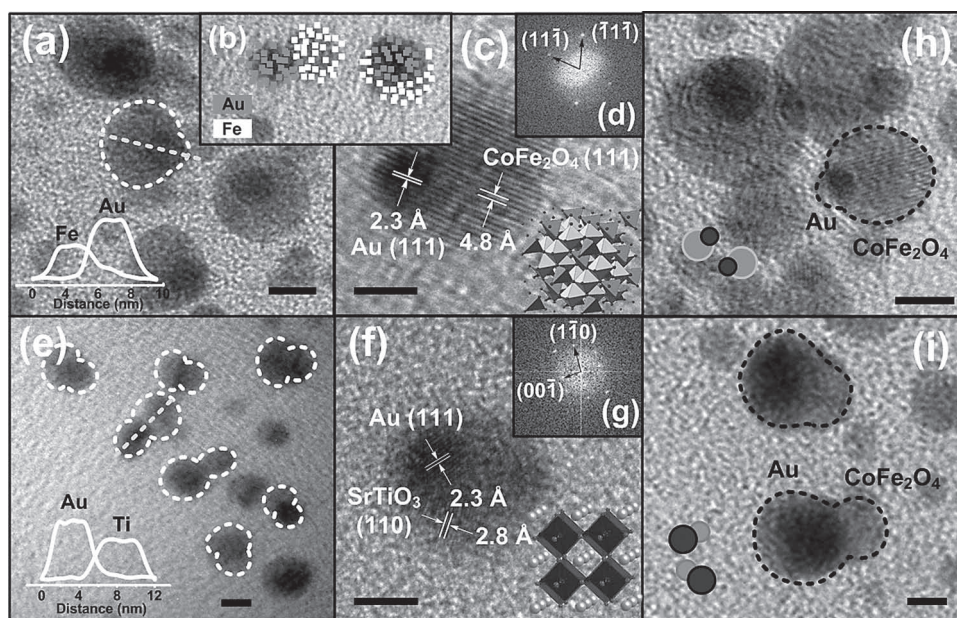

Figure 2. TEM images of as-prepared a)Au–CoFe$_2$O$_4$ and e)Au–SrTiO$_3$, and EDX line analysis of a single heterodimer hybrid particle (marked with white lines). EDX mapping analysis of two7 individual Au–CoFe$_2$O$_4$ heterodimer NPs (b). HRTEM images of an individual Au–CoFe$_2$O$_4$ (c) and its corresponding FFT pattern (d). HRTEM image of isolated SrTiO$_3$ (f) and its corresponding FFT pattern (g). h) and i) demonstrate Au–CoFe$_2$O$_4$ prepared with different sized Au nanoparticles. Scale bars represent 5.0 nm.
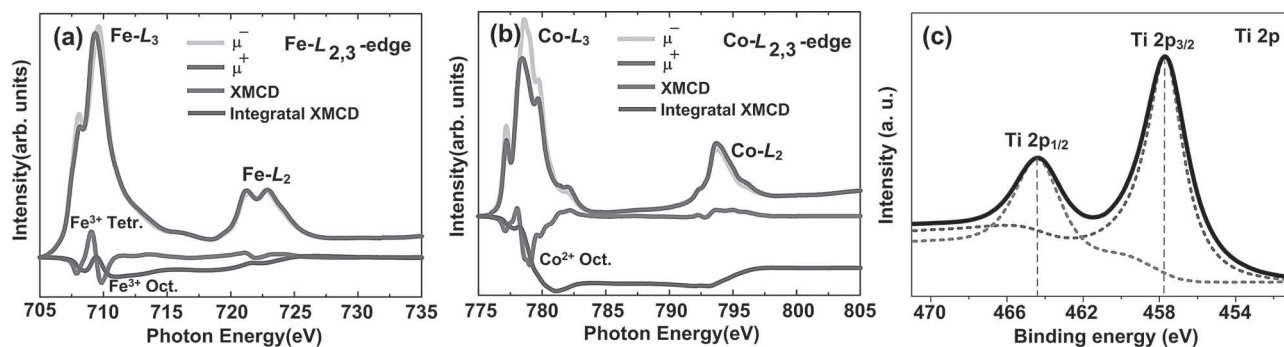
COMMUNICATION

Figure 3. a) Fe-L$_{2,3}$ and b) Co-L$_{2,3}$ spectra of Au–CoFe$_2$O$_4$ heterodimer NPs taken with circularly polarized X-rays at T = 300 K. The photon spin was aligned parallel (μ^+) or antiparallel (μ^-) to the 1 T magnetic field. The corresponding XMCD signal and integration for Au–CoFe$_2$O$_4$ are shown. (c) Binding energies of Ti 2p$_{1/2}$ and Ti 2p$_{3/2}$ of the Au–SrTiO$_3$ sample.

In order to check the valence states and local environments of the complex oxide NPs, we employed synchrotron radiation X-ray absorption spectroscopy (XAS) and X-ray photoelectron spectroscopy (XPS). It can be observed that the spectral line-shape and energy position of the Co-L$_{2,3}$ edge of Au–CoFe$_2$O$_4$ is very similar to what was observed in the CoFe$_2$O$_4$ thin film, as shown in **Figure 3**, indicating Co^{2+} valence states at the octahedral (B) sites.[32] Two sharp peaks at the Fe-L$_3$ edge lie at the same energy as the reference Fe$_2$O$_3$ single crystal demonstrating Fe^{3+} valence states. Figure 3 depicts Co-L$_{2,3}$ (Figure 3a) and Fe-L$_{2,3}$ (Figure 3b) XAS spectra of Au–CoFe$_2$O$_4$ taken with circularly polarized light with the photon spin parallel, μ^+, and antiparallel, μ^-, to the magnetic field. The difference spectrum, $\Delta\mu = \mu^+ - \mu^-$, i.e., the X-ray magnetic circular dichroism (XMCD) spectrum, is also shown in Figure 3. The XMCD spectra are normalized to the main peak of the isotropic spectra at the Co-L$_3$ edge. We obtained ~14% XMCD signal at the Co-L$_3$ edge in Au–CoFe$_2$O$_4$ heterodimer NPs. The spectral line-shape and energy positions of μ^+ and μ^- at the Co-L$_{2,3}$ edge of Au–CoFe$_2$O$_4$ shown in Figure 3b are very similar to what were observed in LaCo$_{0.5}$Mn$_{0.5}$O$_3$, indicating Co^{2+} valence states at the octahedral (B) sites.[33] Note that the XMCD signal in Figure 3a at 709.8 eV that originated from Fe^{3+} at the octahedral site and the XMCD signal at the Co-L$_3$ edge are both negative, reflecting that the Co^{2+} ions and the Fe^{3+} ions residing at the octahedral sites are ferromagnetically coupled.[33] On the other hand, the positive XMCD signal at 709.0 eV demonstrates that the Fe^{3+} ions occupying the tetrahedral sites are antiferromagnetically coupled with Fe^{3+} at octahedral sites. To measure the valence states of Ti cations in Au–SrTiO$_3$ heterodimer NPs, an XPS measurement was performed, as shown in Figure 3c. It can be observed that the binding energies of Ti 2p$_{1/2}$ and Ti 2p$_{3/2}$ are around 464.4 and 457.9 eV, respectively, agreeing with the literature values for SrTiO$_3$.[34]

After establishing structural and chemical information, now we turn to explore the functionalities and interplay of these hybrid nanoparticles. A strong influence on surface plasmon resonance (SPR) of Au NPs conjugated with complex oxide NPs was observed. **Figure 4**a shows the UV-vis spectra of pure Au NPs with different sizes as well as the corresponding Au–CoFe$_2$O$_4$ and Au–SrTiO$_3$ heterodimer NP samples. It can be found that the maxima of the characteristic Au SPR peak shows

a blue-shift from 538 to 525 nm with the size of the Au particles decreasing from 14.2 ± 3.8 to 2.6 ± 1.5 nm. After linking with the CoFe$_2$O$_4$ domain, the SPR peak shows a slight change in its wavelength (red shifted by about 9 nm), while a more pronounced change appears in the case of 14.2 ± 3.8 nm Au–SrTiO$_3$ from 538 to 553 nm, about a 15 nm red-shift. In addition, once attached to the CoFe$_2$O$_4$ domain, the 2.6 ± 1.5 nm Au–CoFe$_2$O$_4$ shows a 13 nm red-shift from that of the pure 2.6 ± 1.5 nm Au NPs. A more dramatic red-shift appears in the case of 2.6 ± 1.5 nm Au–SrTiO$_3$, which was measured to be 565 nm, showing a 40 nm red-shift from that of the 2.6 ± 1.5 nm Au NPs. The SPR absorption cross-section strongly depends on the local dielectric environments. Therefore, the red-shifts of Au hybrids are attributed to the changes of local dielectric environment around the Au domain caused by the complex oxide domains. It is well known that SrTiO$_3$ with a perovskite structure is endowed with a large dielectric constant, and low dielectric loss. Thus, it is reasonable that the Au–SrTiO$_3$ exhibits a more dramatic red-shift of SPR compared with that of Au–CoFe$_2$O$_4$. These results suggest the functionalities of a noble metal can be altered by complex oxide conjugation, which also can be utilized to tailor material properties for functional applications.[4,29]

The interface communication between the nanometer-scale Au domain and the CoFe$_2$O$_4$ domain also leads to the change of magnetization behaviors of the CoFe$_2$O$_4$, especially for the Au-dominant heterodimer sample. Figure 4b shows the magnetization hysteresis loops of the 14.2 ± 3.8 nm Au–CoFe$_2$O$_4$ heterodimer, the 2.62 ± 1.5 nm Au–CoFe$_2$O$_4$ heterodimer, and pure CoFe$_2$O$_4$ NPs generated under equal conditions, respectively. It is evident that the 2.62 ± 1.5 nm Au–CoFe$_2$O$_4$ and 14.2 ± 3.8 nm Au–CoFe$_2$O$_4$ exhibit, respectively, a 20 and 50% lower saturation magnetization than the pure CoFe$_2$O$_4$ NPs. This behavior cannot be fully accounted for by the less than 3% difference in the magnetic volume, but must be explained by a new anisotropy in CoFe$_2$O$_4$ induced by the conjugation of the Au domain. This may be caused by both thermal agitation and the surface spin canting of the CoFe$_2$O$_4$. Due to the inter-linkage of the Au domain, the number of nearest neighbors of Co and Fe atoms at the CoFe$_2$O$_4$ is reduced, which decreases the interatomic exchange coupling. Thus, spins at the interface become canted and saturate at lower magnetization.[35] This provides an effective uniaxial anisotropy much like the surface
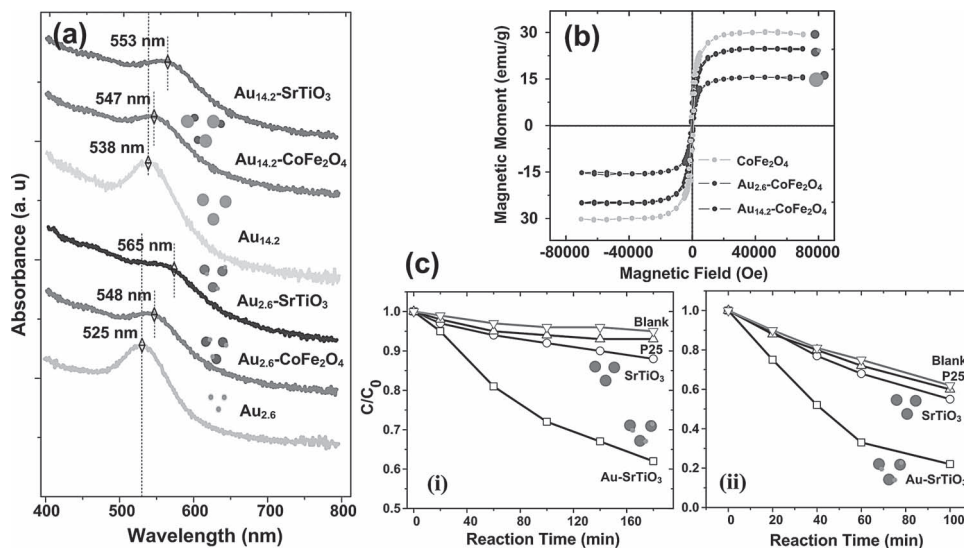
Figure 4. a) UV-Vis spectra of Au NPs with different sizes and the corresponding Au–CoFe$_2$O$_4$ and Au–SrTiO$_3$ heterodimer NP samples. b) Magnetization hysteresis loops measured at 298 K, for assemblies of 8–10 nm CoFe$_2$O$_4$ NPs generated under equal conditions and 14.2 ± 3.8 nm Au–CoFe$_2$O$_4$ heterodimer NPs with a 14.2 ± 3.8 nm Au domain and a 6–8 nm CoFe$_2$O$_4$ domain. c) Photodegradation of rhodamine B (RhB, i) and methyl orange (MO, ii) on commercial TiO$_2$ (P25 aerosol), pure SrTiO$_3$ NPs, and Au–SrTiO$_3$ heterodimer NPs under visible light irradiation (wavelength > 420 nm).

anisotropy in thin films, which dominates the magnetic anisotropy.[36] Accordingly, ferromagnetism could be induced as a result of numerous defects on the product surface, which is well consistent with a previous report by others.[37] Indeed, with a larger size of Au domain, a considerably large absolute number of interfacial sites are expected, which, in turn, may result in an obvious contribution to the change of saturation magnetization due to thermal agitation.

The functionality of SrTiO$_3$ NPs is also strongly affected by the conjugation of an Au domain. The photocatalytic activity of Au–SrTiO$_3$ heterodimer NPs was examined as a demonstration by monitoring the degradation of rhodamine B (RhB) and methyl orange (MO). Figure 4c presents the relationship between the irradiation time and degradation rate of MO catalyzed by commercial TiO$_2$ (P25 aerosol), pure SrTiO$_3$ NPs, and Au–SrTiO$_3$ heterodimer NPs under visible-light irradiation (>420 nm). It can be observed that the Au–SrTiO$_3$ heterodimer exhibits a more active degradation ability for both RhB (Figure 4c–i) and MO (Figure 4c-ii) than that of both pure SrTiO$_3$ and P25. As discussed in the changes of optical properties of Au–SrTiO$_3$, the coherent interaction between the SrTiO$_3$ domain and Au domain can modify the electronic structure of each component. Thus, it is suggestive that the great improvement of photocatalytic activity of SrTiO$_3$ can be ascribed to the recombination of photogenerated electron–hole pairs by Schottky junctions at the Au and SrTiO$_3$ interface.[38] Further investigations on the photocatalytic activity of the Au–SrTiO$_3$ heterodimer are certainly needed with the purpose of understanding the electronic band structure in such nanostructures in more detail.

In summary, as model complex oxide–noble metal hybrids, gold–spinel heterodimer (Au–CoFe$_2$O$_4$) and gold–perovskite heterodimer (Au–SrTiO$_3$) NPs were successfully fabricated and characterized in this study. The properties (optical, magnetic, and photocatalytic) of the composed phases (Au, CoFe$_2$O$_4$, and SrTiO$_3$ domains) strongly depend on the interplay between the

complex oxide and noble metal NPs. These results suggest that the wide range of functionalities in complex oxides can serve to enlarge the playgroup of NP conjugation and create a new pathway to use complex oxide conjugated NPs for applications. For example, with a spinel, i.e., CoFe$_2$O$_4$ domain, one can apply it as a highly sensitive magnetic sensor; with a pervoskite, i.e., a SrTiO$_3$ domain, one can apply it as a high-performance photocatalyst for light energy conversion. The electron deficient Au in the heterodimer structure may be an efficient catalyst for relevant technologically important reactions such as CO oxidation, N$_2$O decomposition, and hydrogeneration.

Experimental Section

Materials Synthesis: A schematic illustration of this process is presented in Figure 1. According to our previously developed biosynthesis of homogeneous Au NP colloids,[24] HAuCl$_4$ was used as the precursor, and bayberry tannin (BT, a soluble and natural polyphenol extracted from the bark of *Myrica rubra*) was applied as both reductant and stabilizer. The reaction was performed at room temperature and finished within 30 s. The size of the Au NPs can be tuned by controlling the concentration of BT. For example, reaction with a low concentration of 100 mg L^{-1} of BT leads to the formation of ca. 6.5 nm Au particles, while reaction with a relatively high concentration of 400 mg L^{-1} of BT results in the growth of ca. 2.5 nm Au particles. The obtained Au particles were then conjugated in situ with the laser-generated ejection of CoFe$_2$O$_4$ and SrTiO$_3$ constituents to form the homogeneous hybrid Au–CoFe$_2$O$_4$ and Au–SrTiO$_3$ heterodimer NPs. Pure-phase CoFe$_2$O$_4$ and SrTiO$_3$ ceramic targets were ablated by a KrF (k = 248 nm) excimer laser with a laser density of 1.2 J cm^{-2}. The laser beam was focused at a 2.0–3.0 mm diameter size below the liquid surface with a spot size of 0.2 mm.

Characterization Techniques: The morphology of the product was observed by using TEM (Tecnai G^2 F20, Netherlands) equipped with a field emission gun operating at 200 kV. TEM samples were prepared by drop-casting the sample suspension onto a carbon-coated copper grid. Raman spectra were recorded in back scattering geometry with a Raman

COMMUNICATION

spectrometer (Raman, HR800, Horiba Jobin-Yvon, France) equipped with a liquid-N_2 cooled back thinned charge couple device (CCD) detector. The output power of the Ar-ion laser operated at 514.5 nm was set at 2.5 mW. The results have been analyzed by fitting the spectra to a Lorentzian line shape. Raman spectra at temperatures below 300 K were obtained using a Raman cell where liquid N_2 passes through a tube located below the samples. A K-type thermocouple in contact with the sample holder in the Raman cell was used for the temperature measurement. The Co- and Fe-$L_{2,3}$ XAS and XMCD spectra were recorded at the Dragon beamline of the National Synchrotron Radiation Research Center (NSRRC) in Taiwan with an energy resolution of 0.25 eV. The sharp peak at 777.2 eV of the Co-L_3 edge of single crystalline CoO and at 709.6 eV of the Fe-L_3 of single crystalline Fe_2O_3 were used for energy calibration, which enabled us to achieve better than 0.05 eV accuracy in the relative energy alignment. The XMCD spectra at both the Co-$L_{2,3}$ and the Fe-$L_{2,3}$ edges were measured at room temperature in a 1 T magnetic field with approximately 80% circularly polarized light. The magnetic field makes an angle of 30° with respect to the Poynting vector of the soft X-rays. The spectra were recorded using the total electron yield method (by measuring the sample drain current) in a chamber with a base pressure of 1×10^{-9} mbar. UV-visible absorption spectra were recorded at room temperature from the spectrophotometer (Shimadzu UV-3600, Japan). Magnetization measurements of the samples were performed on a Quantum Design MPMS-XL5 SQUID magnetometer at 300 K.

Supporting Information

Supporting Information is available from the Wiley Online Library or from the author.

Acknowledgements

[1] C. T. Campbell, *Science* **2004**, *306*, 234.
[2] J. Perez-Juste, I. Pastoriza-Santos, L. M. Liz-Marzán, P. Mulvaney, *Coord. Chem. Rev.* **2005**, *249*, 1870.
[3] S. C. Glotzer, M. J. Solomon, *Nat. Mater.* **2007**, *6*, 557.
[4] E. V. Shevchenko, M. I. Bodnarchuk, M. V. Kovalenko, D. V. Talapin, R. K. Smith, S. Aloni, W. Heiss, A. P. Alivisatos, *Adv. Mater.* **2008**, *20*, 4323.
[5] A. Ohnuma, E. C. Cho, P. H. C. Camargo, L. Au, B. Ohtani, Y. N. Xia, *J. Am. Chem. Soc.* **2009**, *131*, 1352.
[6] M. Grzelczak, J. Vermant, E. M. Furst, L. M. Liz-Marzán, *ACS Nano* **2010**, *4*, 3591.
[7] S. Dowland, T. Lutz, A. Ward, S. P. King, A. Sudlow, M. S. Hill, K. C. Molloy, S. A. Haque, *Adv. Mater.* **2011**, *23*, 2739.
[8] H. Yu, M. Chen, P. Rice, S. Wang, R. White, S. Sun, *Nano Lett.* **2005**, *5*, 379.
[9] R. J. Zeches, M. D. Rossell, J. X. Zhang, A. J. Hatt, Q. He, C. H. Yang, A. Kumar, C. H. Wang, A. Melville, C. Adamo, *Science* **2009**, *326*, 977.
[10] S. Y. Yang, J. Seidel, S. J. Byrnes, P. Shafer, C. H. Yang, M. D. Rossell, P. Yu, Y. H. Chu, J. F. Scott, J. W. Ager, *Nat. Nanotechnol.* **2010**, *5*, 143.
[11] Y. H. Chu, L. W. Martin, M. B. Holcomb, M. Gajek, S. J. Han, Q. He, N. Balke, C. H. Yang, D. Lee, W. Hu, *Nat. Mater.* **2008**, *7*, 478.
[12] H. Zheng, F. Straub, Q. Zhan, P. L. Yang, W. K. Hsieh, F. Zavaliche, Y. H. Chu, U. Dahmen, R. Ramesh, *Adv. Mater.* **2006**, *18*, 2747.
[13] K. Yamaura, Q. Huang, L. Zhang, K. Takada, Y. Baba, T. Nagai, Y. Matsui, K. Kosuda, E. Takayama-Muromachi, *J. Am. Chem. Soc.* **2006**, *128*, 9448.
[14] M. V. Kovalenko, M. I. Bodnarchuk, R. T. Lechner, G. Hesser, F. Schäffler, W. Heiss, *J. Am. Chem. Soc.* **2007**, *129*, 6352.
[15] V. Corral-Flores, D. Bueno-Baqués, R. F. Ziolo, *Acta Mater.* **2010**, *58*, 764.
[16] D. Tang, R. Yuan, Y. Chai, H. An, *Adv. Funct. Mater.* **2007**, *17*, 976.
[17] Q. Dai, D. Berman, K. Virwani, J. Frommer, P. O. Jubert, M. Lam, T. Topuria, W. Imaino, A. Nelson, *Nano Lett.* **2010**, *10*, 3216.
[18] M. B. Katz, G. W. Graham, Y. Duan, H. Liu, C. Adamo, D. G. Schlom, X. Pan, *J. Am. Chem. Soc.* **2011**, *133*, 18090.
[19] J. Y. Son, G. Lee, M. H. Jo, H. Kim, H. M. Jang, Y. H. Shin, *J. Am. Chem. Soc.* **2009**, *131*, 8386.
[20] K. Yamaura, Y. Shirako, H. Kojitani, M. Arai, D. P. Young, M. Akaogi, M. T. Nakashima, T. Katsumata, Y. Inaguma, E. Takayama-Muromachi, *J. Am. Chem. Soc.* **2009**, *131*, 2722.
[21] P. M. Shirage, K. Kihou, C. H. Lee, H. Kito, H. Eisaki, A. Iyo, *J. Am. Chem. Soc.* **2011**, *133*, 9630.
[22] C. Y. Meng, H. Chen, P. Wang, L. Chen, *Chem. Mater.* **2011**, *23*, 4910.
[23] T. H. Shin, S. Ida, T. Ishihara, *J. Am. Chem. Soc.* **2011**, *133*, 19399.
[24] L. Ju, T. Sabergharesou, K. G. Stamplecoskie, M. Hegde, T. Wang, N. A. Combe, H. Wu, P. V. Radovanovic, *J. Am. Chem. Soc.* **2012**, *134*, 1136.
[25] Z. Dong, T. Ye, T. Yu J. Zhao, F. Wang, L. Zhang, X. Wang, S. Guo, *J. Mater. Chem.* **2011**, *21*, 5978.
[26] X. Huang, H. Wu, X. Liao, B. Shi, *Green Chem.* **2010**, *12*, 395.
[27] K. Y. Niu, J. Yang, S. A. Kulinich, J. Sun, H. Li, X. W. Du, *J. Am. Chem. Soc.* **2010**, *132*, 9814.
[28] F. Lin, J. Yang, S. H. Lu, K. Y. Niu, Y. Liu, J. Sun, X. W. Du, *J. Mater. Chem.* **2010**, *20*, 1103.
[29] Q. C. Sun, C. S. Birkel, J. Cao, W. Tremel, J. L. Musfeldt, *ACS Nano* **2012**, *6*, 4876.
[30] C. Altavilla, M. Sarno, P. Ciambelli, *Chem. Mater.* **2009**, *21*, 4851.
[31] J. Guo, X. Wang, P. Miao, X. Liao, W. Zhang, B. Shi, *J. Mater. Chem.* **2012**, *22*, 11933.
[32] J. A. Moyer, C. A. F. Vaz, D. A. Arena, D. Kumah, E. Negusse, V. E. Henrich, *Phys. Rev. B* **2011**, *84*, 054447.
[33] T. Burnus, Z. Hu, H. H. Hsieh, V. L. J. Joly, P. A. Joy, M. W. Haverkort, Hua Wu, A. Tanaka, H. J. Lin, C. T. Chen, L. H. Tjeng, *Phys. Rev. B* **2008**, *77*, 125124.
[34] H. Yu, S. Ouyang, S. Yan, Z. Li, T. Yu, Z. Zou, *J. Mater. Chem.* **2011**, *21*, 11347.
[35] B. Martinez, X. Obradors, L. Balcells, A. Rouanet, C. Monty, *Phys. Rev. Lett.* **1998**, *80*, 181.
[36] J. A. Moyer, D. P. Kumah, C. Vaz, D. A. Arena, V. E. Henrich, *Appl. Phys. Lett.* **2012**, *101*, 21907.
[37] H. Yu, M. Chen, P. M. Rice, S. X. Wang, R. L. White, S. Sun, *Nano Lett.* **2005**, *5*, 379.
[38] Z. Jiang, F. Zou, X. Qin, L. Jiang, J. Zhi, T. Xiao, P. P. Edwards, *Chem. Commun.* **2012**, *48*, 8514.